

Recent progress in hydrodynamic characteristics research and application of annular centrifugal extractors

Hang Yang¹, Xiaoyong Yang¹, Xiao Dong¹, Zhaojin Lu¹, Zhishan Bai (✉)¹, Yinglei Wang², Fulei Gao²

¹ School of Mechanical and Power Engineering, East China University of Science and Technology, Shanghai 200237, China

² Xi'an Modern Chemistry Research Institute, Xi'an 710000, China

© Higher Education Press 2022

Abstract The annular centrifugal extractor (ACE) integrates mixing and separation. It has been widely used in many industrial fields because of its low residence time, compact structure, and high mass transfer efficiency. Most of the literature has focused on flow instabilities, flow visualization, and computational fluid dynamics simulations. More recently, research on hydrodynamic behavior and structural optimization has received widespread attention. With the development of ACE technology, applications have been broadened into several new areas. Hence, this paper reviews research progress regarding ACE in terms of hydrodynamic characteristics and the structural improvements. The latest applications covering hydrometallurgy, nuclear fuel reprocessing, bio-extraction, catalytic reaction, and wastewater treatment are presented. We also evaluate future work in droplet breakup and coalescence mechanisms, structural improvements specific to different process requirements, scaling-up methods, and stability and reliability after scaling-up.

Keywords annular centrifugal extractor, hydrodynamic characteristics, structure optimization, the latest application

1 Introduction

Solvent extraction is suitable for large-scale production owing to its high separation efficiency and easy operation. Common solvent extraction equipment includes mixer-settler, extraction column, and centrifugal extractor. Compared with the extraction column and mixer-settler, the annular centrifugal extractor (ACE) has a compact structure, high mass transfer efficiency, low residence time, low hold-up, and rapid separation speed. Therefore,

it is widely used in various industries, including the chemical industry [1,2], biomedicine [3–6], hydrometallurgy [7,8], and nuclear fuel reprocessing [9,10].

The ACE realizes mass transfer and two-phase liquid–liquid separation by employing a centrifugal force field. The early developed centrifugal extractor had a complex structure, high processing requirements, expensive manufacturing cost, and inconvenient maintenance [11]. Hence, its application was limited. In the 1970s, the Argonne National Laboratory developed the first ACE with simple manufacturing and operation [12]. A typical ACE structure is shown in Fig. 1 and is characterized by a hanging rotor. The two-phase liquid enters the annular region from the two inlets, respectively. Intense mixing and mass transfer occur under the action of shear force as generated by a high-speed rotating cylinder. The mixture enters the interior of the rotor through a channel under the bottom of the rotor. The mixture is then gradually separated while flowing from the bottom to the top of the rotor.

Most of the studies related to ACE have focused on flow instabilities, flow visualization, and computational fluid dynamics (CFD) simulations. Recent studies on hydrodynamic behavior and structural optimization have started to receive attention. Hydrodynamic studies such as dispersed phase hold-up and droplet size distribution are vital for evaluating mass transfer coefficients and separation efficiency. Many structural improvements have also been performed for specific process requirements and improved mass transfer performance. The development of ACE technology has broadened the applications into several new areas. Existing reviews focused on ACE technology include Taylor-vortex flow in the annulus [13], CFD simulations of flow pattern [14], advances in the development of structures and equipment [15], and hydraulic operation [16]. Given the current state of affairs, a review of the hydrodynamic behavior, structure optimization, and recent application of ACE are of great importance. Here, we summarize recent research progress

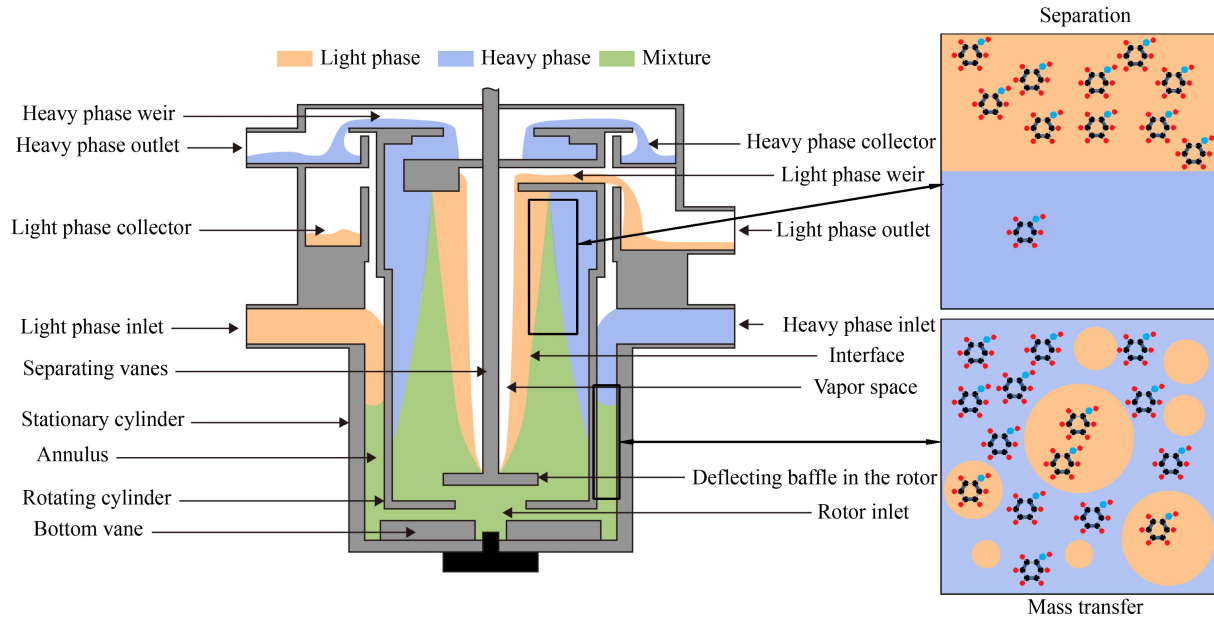


Fig. 1 Schematic diagram of the ACE.

about hydrodynamic characteristics. We introduce some structural modifications to improve the mixing and separation performance in specific industrial applications. In addition, recent applications of ACE within hydrometallurgy, nuclear fuel reprocessing, bioextraction, catalytic reactions, and wastewater treatment are presented.

2 Hydrodynamic characteristics of ACE

The hydrodynamic characteristics of ACE are the basis for ACE design, optimization, and scale-up; they are important for evaluating mass transfer. The hydrodynamic characteristics of ACE have been extensively investigated including dispersed phase hold-up, two-phase flow pattern, droplet size distribution, and residence time distribution (RTD) (Fig. 2). These behaviors depend on parameters such as rotational speed, flow ratio, total throughput, extractant concentration, pH value, fluid density, and fluid viscosity. This section reviews the research progress of hydrodynamic characteristics and their prediction models in recent years.

2.1 Flow patterns

2.1.1 Flow patterns in the annular region

Two-phase flow in the annular region has always been of particular interest to researchers owing to the vast application of ACE and its complexity. Accurate determinations and identification of the two-phase flow pattern and its transition inside an ACE is essential theoretical guidance for understanding the hydrodynamic characteristics and further design optimization. The macroscopic characteristics of two-phase Taylor–Couette flows have

been extensively studied since the 1980s. The main research areas include flow pattern identification, flow pattern mapping, flow pattern transformation, and prediction. These flow patterns are mainly affected by operating parameters, geometric parameters, and physical properties of the system including rotational speed, annular size, interfacial tension, and density difference. Joseph et al. [17] were the first to investigate the flow regime of two-phase immiscible liquid inside the annulus—they observed emulsion flow, roller flow, band flow, and phase inversion. The band flow is the limit state of roller flow where the interface breaks and contacts two cylinders.

Campero and Vigil [18] observed three distinct flow patterns: banded flow, spatially homogeneous flow, and oscillatory flow between the first two types of flow patterns. They established empirical formulas describing the transition boundaries between these different flow patterns using Reynolds number (Re) and Weber number (We). Photographic evidence suggests that the banded flow is caused by migration of organic droplets into the vortex core. The transition boundary of the banded flow can be described by a critical equation (Eq. (1)) based on the characteristic time scale [19]:

$$\frac{\tau_c}{\tau_p} = \frac{18\mu_c\mu_p}{(\rho_c - \rho_p)\rho_c d_p^2 u_\theta^2}. \quad (1)$$

Here, τ_c is the characteristic time for droplets to migrate from the vortex boundary to the vortex core due to centrifugal force; τ_p is the characteristic time for droplets to migrate from the vortex core to the vortex boundary due to turbulent dispersion; μ_c is the continuous phase viscosity; μ_p is the turbulent viscosity; ρ_c is the continuous phase density; ρ_p is the dispersed phase density; u_θ is the circumferential angular velocity of droplets with the vortex core as the rotation axis; and d_p is the average

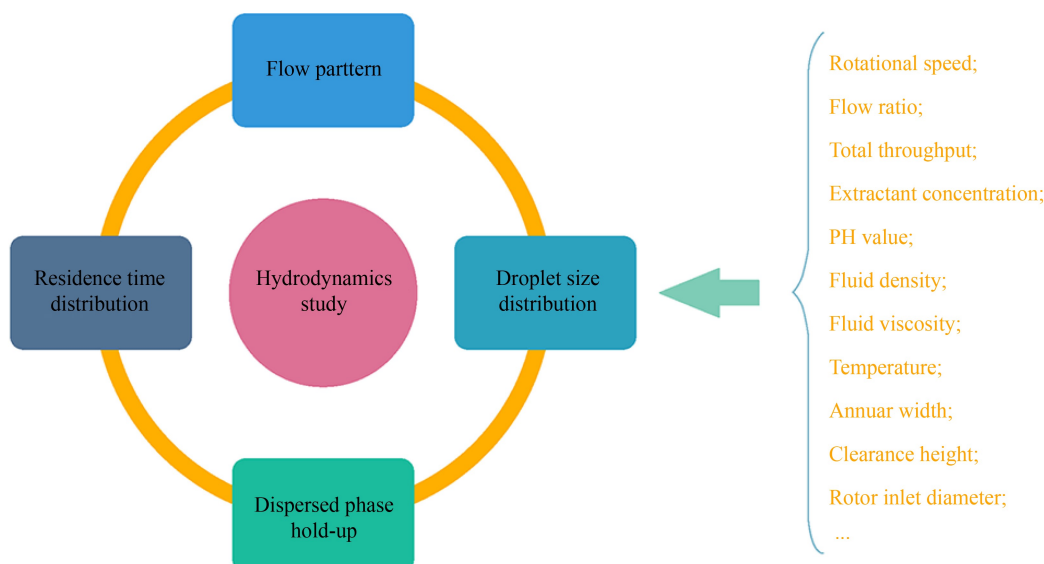


Fig. 2 Hydrodynamic studies parameters and factors affecting the hydrodynamics of ACE.

droplet diameter.

The liquid–liquid two-phase flow exhibits different flow patterns in the horizontal annular region such as stratified flow, banded flow, and homogeneous flow. In the vertical annulus, the vertical system shows another flow pattern due to the gravitational field. This is called segregated dispersion flow and occurs at relatively low rotational speeds versus banded flow and homogeneous flow [20]. Figure 3 shows four distinct flow patterns inside a closed vertical Taylor reactor including stratified flow at relatively low rotational speeds. As the rotational speed increases, the interface between oil and water phases moves upward. At a certain rotational speed, the interface starts to oscillate and eventually breaks up with oil droplets dispersed in the water phase flowing in the bottom, whereas water droplets dispersed in the oil phase flowing in the top, thus eventually forming a segregated dispersion. For larger droplets, the centrifugal force generated by the tangential rotation of the fluid around the inner cylinder caused band dispersion as the rotational speed was further increased. A homogeneous dispersion was observed in the case of smaller droplets and two-phase density differences. The two-phase flow pattern also shifted from a horizontally banded flow to a helical flow when the upward flow of the organic phase breaks the confinements of the Taylor vortex inside the annulus [21,22]. These two-phase flow patterns in the annulus from the literature are summarized in Table 1.

2.1.2 Flow patterns in the separation region

The ACE separation zone consists of the rotor and the upper weir. Since the upper part and the outlet are in direct contact with air, the flow pattern in the rotor is a gas–liquid–liquid three-phase flow. Figure 1 shows that the mixture enters the rotor through the rotor inlet and is thrown to the wall under the centrifugal action of the

spinning rotor. The less-dense air is concentrated in the center of the rotor to form an air column. The flow pattern and phase interface within the rotor significantly affect the separation performance of the liquid–liquid phases. Since the rotor is located inside the mixing chamber, it is difficult to observe the flow pattern inside the rotor by conventional experimental methods. Thus, researchers have mostly used numerical simulations or experimental measurements of simplified ACE models to investigate the flow inside the rotor [26–28]. As shown in Fig. 4, the flow pattern inside the rotor has a gas–liquid interface with a parabolic surface at lower speeds and an approximately conical surface at higher speeds [29]. This is because the centrifugal force is much higher than the gravitational force when the speed is high. The simulation results of Li et al. [30] showed that the organic–water phase interface was a parabola parallel to the gas–liquid interface in the closed inlet mode and a cylinder in the open inlet mode. The separated two phases of liquid pass through their respective weirs and flow as droplets or streams at different flow rates and operating conditions, respectively [31].

2.2 Dispersed phase hold-up

The interfacial area of mass transfer in the extraction process depends on the dispersed phase hold-up ϕ and the mean droplet diameter $d_{3,2}$. Therefore, study of the dispersed phase hold-up is vital for evaluating the mass transfer performance. As depicted in Eq. (2), the dispersed phase hold-up is defined as the ratio of the dispersed phase volume V_d to the total liquid phase volume ($V_c + V_d$) for liquid–liquid mixing systems.

$$\phi = \frac{V_d}{V_d + V_c} \quad (2)$$

As ϕ increases, mass transfer interfacial area increases,

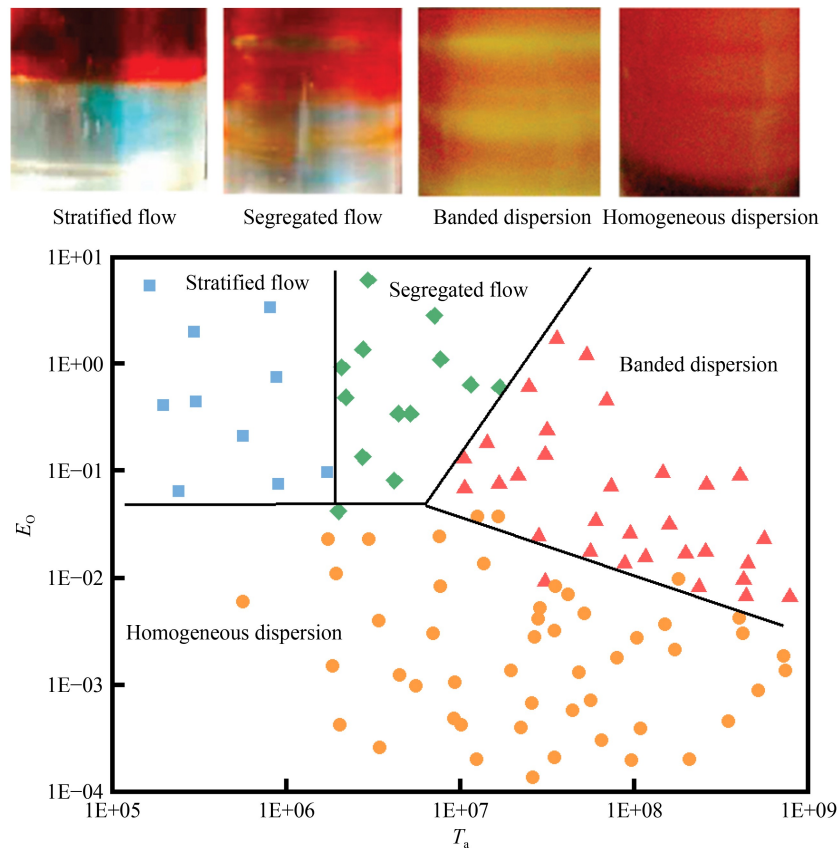


Fig. 3 Flow pattern and flow map in a closed vertical Taylor–Couette device. Reprinted with permission from Ref. [20], copyright 2010, American Chemical Society.

Table 1 Liquid–liquid two-phase flow pattern in the annulus ^{a)}

Sr. no.	Rotation		Orientation	Flow pattern	Method	Ref.
	Inner	Outer				
1	✓		Horizontal	(1) Emulsion flow, (2) roller flow, and (3) banded flow	Oil phase dyeing + photography	[17]
2	✓		Horizontal	(1) Banded flow, (2) spatially homogeneous flow, and (3) oscillatory flow between (1) and (2)	Oil phase dyeing + photography	[18]
3	✓	✓	Horizontal	(1) Two-layer flow and (2) “barber pole” pattern	LIF ^{a)} + video	[23]
4	✓		Horizontal	(1) Banded flow and (2) homogeneous flow	Oil phase dyeing + video	[19]
5	✓		Vertical	(1) Stratified flow, (2) segregated dispersion, (3) banded dispersion, and (4) homogeneous dispersion	Fluent + PLIF ^{b)} + high speed photography	[20]
6	✓		Vertical	(1) Spiral flow, (2) ring flow, and (3) ring flow with emulsion.	Fluent + ultrasonic velocity profiling	[24]
7	✓		Vertical	(1) Disordered droplet flow, (2) banded droplet flow, and (3) flooding	Oil phase dyeing + video	[25]
8	✓		Vertical	(1) Pseudo-homogenous flow, (2) weakly banded flow, (3) horizontally banded flow, and (4) helical flow	Oil phase dyeing + video	[21]

a) LIF: Laser induced fluorescence; b) Planar laser induced fluorescence.

thus leading to an increase in the number of droplets. The rapid coalescence and redistribution of droplets lead to an increase in the mass transfer coefficient. Therefore, relatively high dispersed phase hold-up is beneficial for mass transfer. However, there is a limit to the dispersed phase hold-up under continuous operating conditions, and phase conversion occurs beyond this limit. Factors affecting the ϕ include flow ratio, input power (rotational speed), two-phase properties, and geometry. The ϕ

decreases with increasing flow ratio (continuous phase/dispersed phase) and increases with increasing power per unit volume and continuous phase viscosity [32,33]. The negligible effect of the density difference between the two phases on ϕ can be attributed to the minimal slip velocity and the effect of turbulent vortices.

Several related correlations for ϕ have been proposed as shown in Table 2. Davis and Weber [34] proposed a correlation for ϕ between rotating cylinders that is a

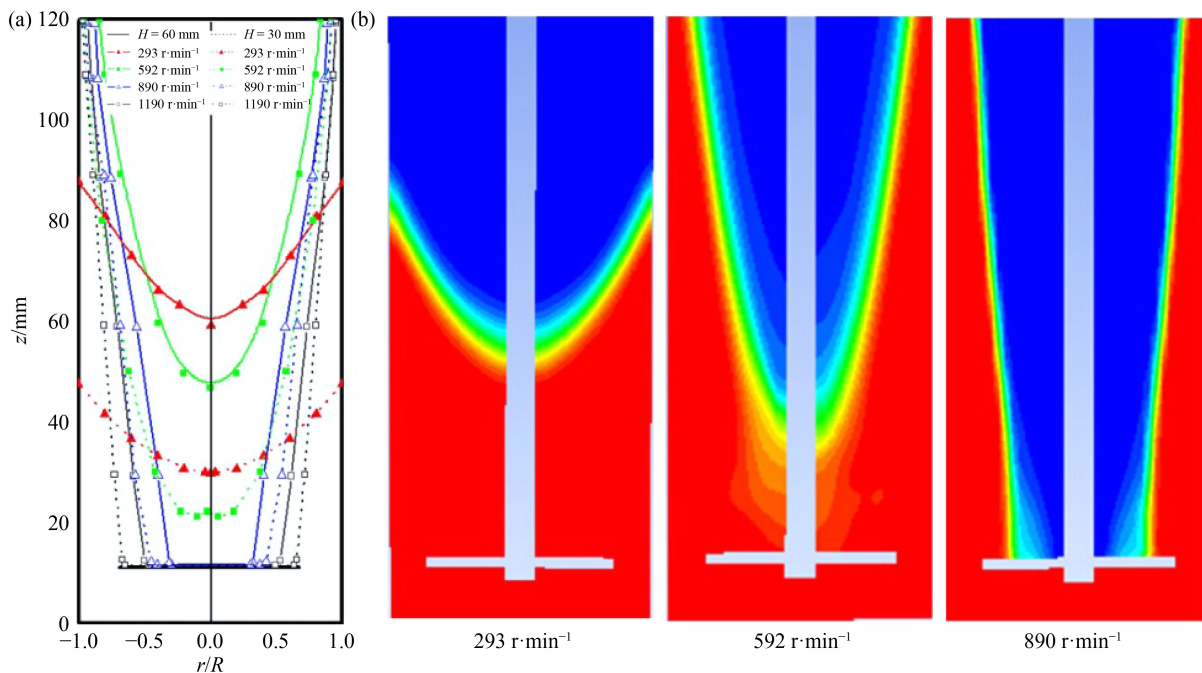


Fig. 4 Water-vapor interface in the rotor zone at different rotational speeds. (a) PIV; (b) CFD. Reprinted with permission from Ref. [29], copyright 2019, East China University of Science and Technology.

Table 2 Related correlation of dispersed phase hold-up ^{a)}

Correlation	Geometry/mm	System/system physical property	Ref.
$\phi = C_2 \left(\frac{\omega r_m^{0.5} \Delta r^{1.5} \rho_C r_i}{r_0 \mu_C} \right)^2 \frac{V_D^{0.5}}{\Delta r^3}$	$15.2 < D < 35$ $1 < \Delta r < 3.5$	2.5% TBP ^{a)} in ultrasene/ $0.0042 \text{ mol} \cdot \text{L}^{-1}$ uranyl nitrate in $5 \text{ mol} \cdot \text{L}^{-1} \text{ HNO}_3$	[34]
$\phi = G \left[C_1 + C_2 \left(\frac{(v_c + v_d)}{dRn} \right)^3 \right] \left(\frac{1}{We} \right)^{0.673} \left(\frac{1}{Fr} \frac{\Delta p}{\rho_c} \right)^{-2.177}$	$D = 50$ $\Delta r = 25$	ShellSol T/water	[35]
$\phi = 0.583 \left(\frac{P}{V} \right)^{0.11} \left(\frac{Q_D}{Q_C + Q_D} \right)^{0.93} \left(\frac{\sigma^3 \Delta \rho}{\mu_C^4 g} \right)^{-0.03} \left(\frac{\mu_D}{\mu_C} \right)^{-0.04}$	$30 < D < 250$ $2 < \Delta r < 25$	$50 < \Delta \rho < 600 \text{ kg} \cdot \text{m}^{-3}$ $2.2 < \sigma < 58 \text{ mN} \cdot \text{m}^{-1}$ $1 < \mu_c < 6.5 \text{ mPa} \cdot \text{s}^{-1}$ $0.7 < \mu_d < 27 \text{ mPa} \cdot \text{s}^{-1}$	[33]

a) Tri-n-butyl phosphate.

function of operating parameters such as rotational speed and superficial velocity of the dispersed phase as well as geometric parameters and the physical properties of the continuous phase. Grafschafter and Siebenhofer [35] proposed a correlation for ϕ within a Taylor–Couette disc contactor. It is a function of the operating parameters, a dimensionless number, and physical properties. However, the above correlations were obtained in the liquid-filled annular region, and the dispersed phase hold-up in ACE is different. Kadam et al. [33] proposed a correlation for ϕ in ACE that considered the effects of the operating parameters and the physical properties of the liquid.

The ϕ distribution inside the ACE was obtained using numerical simulations (Fig. 5). The results showed the difference in dispersed phase hold-up distribution between the annulus and rotor. However, the simulation results did not consider the effect of vapor space, and thus the value of the dispersed phase hold-up from the simulation in the rotor is higher than that obtained in the actual operating situation [36]. Currently, ϕ is mostly an overall mean value obtained by the direct sampling

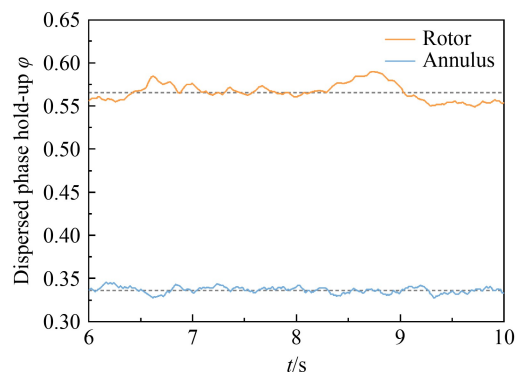


Fig. 5 Dispersed phase hold-up in the annular region and in the rotor region. Reprinted with permission from Ref. [36], copyright 2021, Elsevier.

method. The ϕ distribution at different locations is still mainly obtained by numerical simulations. Therefore, flow field testing techniques (e.g., planar laser induced fluorescence) should be considered in the future to obtain a ϕ distribution at different regions.

2.3 Droplet size distribution

In an ACE, the shearing force caused by the rotating inner cylinder in the narrow annular region causes the two-phase liquid to mix: one phase is dispersed into the other phase in the form of droplets. The study of droplet size and distribution has vital significance for improving the mass transfer performance of the extractor. A smaller droplet size leads to a larger liquid–liquid interface area and a higher mass transfer efficiency. In addition, the subsequent phase separation process will also be affected by droplet size. Excessively small droplets will lead to emulsification, thus making separation of the two phases difficult and resulting in phase entrainment. Therefore, the operating and geometric parameters should be adjusted to keep the droplet size in the optimal range to ensure excellent mass transfer and separation performance of the ACE. Currently, most of the studies aim to find the critical factors affecting droplet breakup to predict the droplet size distribution in the extractor. These studies can be divided into two categories: (1) direct measurements of droplet size distributions without addressing the exact mechanism leading to droplet breakup; (2) single droplet experiments to determine the breakup and coalescence mechanism for the population balance equation.

2.3.1 Droplet size distribution characteristics

The droplet size and distribution strongly influence the mass transfer performance and dispersion of the two-phase fluid; thus, quickly and accurately measuring the diameter and size distribution of the droplets has also received extensive attention. Current methods for measuring the droplet size distribution in the ACEs include contact and non-contact measurements. Non-contact measurement methods include a high-speed camera and phase Doppler particle analyzer (PDPA). Contact measurement includes focused beam reflectance measurement (FBRM), microscopic measurement, and laser-based drop size analyzer measurement. If the non-contact method can provide good visual observation, then the error of the

contact type (tool interference) is higher than that of the “non-contact type”. Table 3 summarizes the droplet size measurement methods and measurement results in the ACEs and Taylor–Couette devices.

The droplet swarms in the extraction equipment is a system with a wide distribution of droplet diameters. The mean diameter of the droplets in the ACEs can be presented by the Sauter mean diameter $d_{3,2}$ based on the volume-to-area ratio for n droplets:

$$d_{3,2} = \frac{\sum_{i=1}^n d_i^3}{\sum_{i=1}^n d_i^2}, \quad (3)$$

where d_i is the drop diameter. The main factors affecting the droplet size distribution are the dispersed phase hold-up, two-phase flow ratio, power consumption per unit volume, interfacial tension and continuous phase viscosity, and surface properties of the rotor [33,40,41,43–45]. Through numerous experimental studies, scientists have obtained the correlations between the mean droplet diameter and system properties (such as dynamic viscosity and interfacial tension), geometry (such as the width of the annular gap), and operating conditions (such as the rotational speed of the inner cylinder, input power, and hold-up); some of the main correlations are shown in Table 4. Generally speaking, different correlations have a specific range of applications and need to be carefully selected according to different working conditions and systems.

The droplet size number distribution within the ACE conforms to a log-normal distribution, and the cumulative size distribution conforms to a Rosin–Rammler distribution [37,40]. Figure 6 shows the experimental apparatus for droplet size measurement and the droplet size distribution in ACE. Figures 6(c) and 6(d) show the size distribution and mean particle size of the ring gap droplets at different rotor speeds: the distribution width becomes significantly narrower, and the mean droplet size decreases rapidly as the rotor speed increases. The droplet size distributions ranged from 40 μm to 1 mm. At

Table 3 Measurement method of droplet size in the annulus ^{a)}

Method	System/system physical property	Mean droplet size range/ μm	Ref.
Image analysis	PDMS ^{a)} /water	100–400	[37]
	Kerosene/water	1200–2600	[20]
	Hexane/water	900–2700	[38]
	40% TBP in dodecane/37.5% Al(NO ₃) ₃ in 1 mol·L ^{−1} HNO ₃	58–107	[39]
PDPA	0.013 < σ < 0.033 N·m ^{−1} 85.1 < $\Delta\rho$ < 219.37 kg·m ^{−3} 0.00072 < μ_d < 0.032 Pa	28–206	[40]
FBRM	1,2-dichloroethane/water	50–600	[41]
Laser-based drop size analyzer	30% TBP in dodecane/0.1 mol·L ^{−1} HNO ₃	30–80	[42]
Calculation from dispersed phase hold-up and effective interfacial area	50 < $\Delta\rho$ < 600 kg·m ^{−3} 2.2 < σ < 58 mN·m ^{−1}	8–55	[33]

a) polydimethylsiloxane.

3000 r·min⁻¹, the Sauter mean droplet diameter is close to 200 μm. The droplet size distribution is wider near the free surface in the mixing zone and narrower in the bottom, i.e., the vane region (Fig. 6(b)) [37].

2.3.2 Breakup and coalescence of droplets

Droplet breakup occurs mainly in the annular region because of the shear stress and turbulence generated by the spinning inner cylinder. Droplet coalescence mainly occurs inside the rotor due to the centrifugal force induced by the high-speed rotation of the rotor. The breakup and coalescence of droplets in a liquid–liquid

dispersion system can significantly affect the mass transfer rate and separation efficiency of ACE.

The droplet coalescence model and breakup model are two key models that describe droplet coalescence and breakup. The most famous breakup model is from Coualoglou–Tavlarides [48]. They considered the influence of pressure fluctuations on droplet breakup in an isotropic flow field and established a droplet breakup model:

$$g(d) = c_1 \frac{\varepsilon^{1/3}}{d^{2/3}(1+\phi)} \cdot \exp \left[-c_2 \frac{\sigma(1+\phi)^2}{\rho_d \varepsilon^{2/3} d^{5/3}} \right]. \quad (4)$$

For droplet dispersion in a turbulent Taylor vortices, Eskin et al. [49] modified the Coualoglou–Tavlarides

Table 4 Principal correlation of Sauter mean droplet diameter in the annular region

Sr. no.	Correlation	Geometry/mm	System/system physical property	Ref.
1	$\frac{d}{D} = 150(We)^{-0.65}(Re)^{-0.2} \left(\frac{\mu_d}{\mu_c} \right)^{0.5} \left(\frac{D}{ID} \right)^{0.5}$	$27 < D < 32$, $1.58 < \Delta r < 3.38$	$790 < \rho_c < 1380 \text{ kg} \cdot \text{m}^{-3}$, $9 < \sigma < 34 \text{ mN} \cdot \text{m}^{-1}$, $0.45 < \mu_d < 70 \text{ mPa} \cdot \text{s}^{-1}$	[46]
2	$d_{3,2} = 2.2 \times 10^{-2} \left(\frac{P}{V} \right)^{-0.33} (\rho_c)^{-0.19} \sigma^{0.6} \left(\frac{\mu_d}{\mu_c} \right)^{0.1} (1 + 8.5\phi)$	$30 < D < 250$, $2 < \Delta r < 25$	$50 < \Delta \rho < 600 \text{ kg} \cdot \text{m}^{-3}$, $2.2 < \sigma < 58 \text{ mN} \cdot \text{m}^{-1}$, $1 < \mu_c < 6.5 \text{ mPa} \cdot \text{s}^{-1}$, $0.7 < \mu_d < 27 \text{ mPa} \cdot \text{s}^{-1}$	[33]
3	$d_d = 0.145 \left(\frac{\mu_c}{\nu_d} \right)^{0.4} (\sigma)^{1.43} \left(\frac{P}{V} \right)^{-0.39} (1 + \phi)^{3.33}$	$D = 39$, $5.5 < \Delta r < 10.5$	$85.1 < \Delta \rho < 219.37 \text{ kg} \cdot \text{m}^{-3}$, $0.013 < \sigma < 0.033 \text{ N} \cdot \text{m}^{-1}$, $0.72 < \mu_d < 32 \text{ mPa} \cdot \text{s}^{-1}$	[40]
4	$\frac{D_{32}^{(v)}}{l_m} = 0.08 We^{-\frac{3}{5}} \left(1 + 9.9 \left(\frac{\rho_c}{\rho_d} \right)^{\frac{1}{2}} \frac{\mu_d}{\gamma} (D_{32} l_m^2 \gamma^3)^{\frac{1}{3}} \right)^{\frac{3}{5}}$	$D = 225$, $\Delta r = 7.5$	$82 < \Delta \rho < 238 \text{ kg} \cdot \text{m}^{-3}$, $0.0159 < \sigma < 0.0237 \text{ N} \cdot \text{m}^{-1}$, $0.00049 < \mu_d < 0.07 \text{ kg} \cdot \text{m}^{-1} \cdot \text{s}^{-1}$	[47]

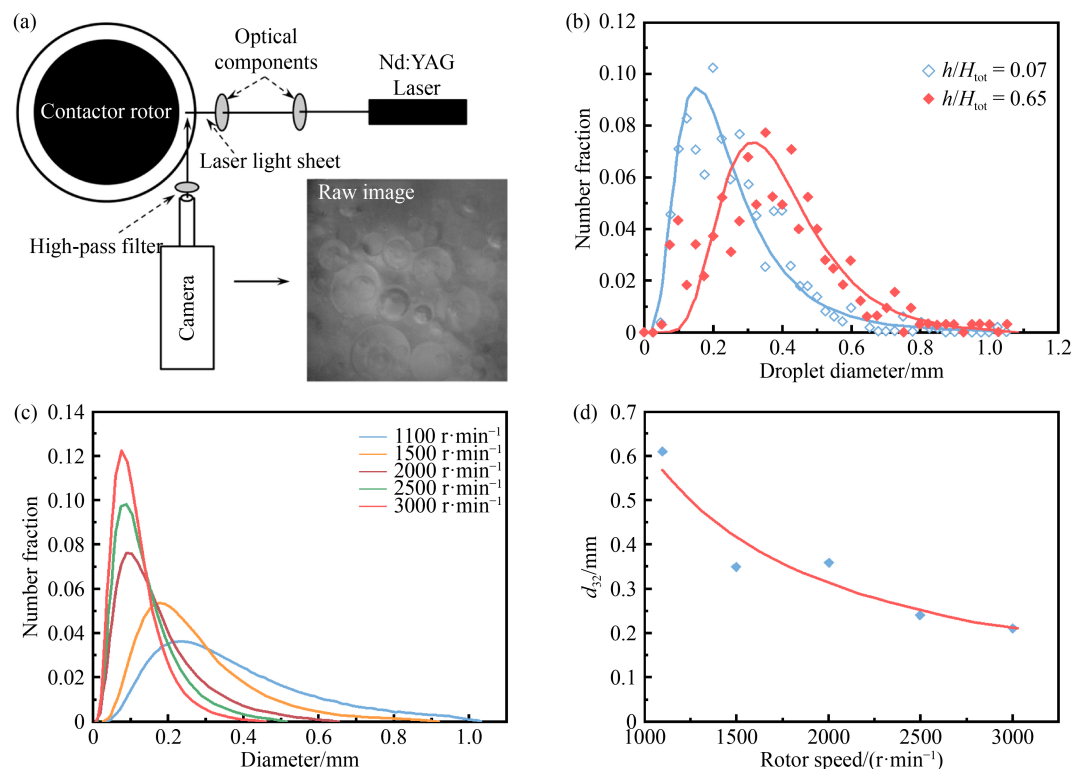


Fig. 6 (a) Schematic illustration for droplet size measurement; (b) droplet size distribution at different locations of ACE; (c) droplet size distribution at different rotational speeds; (d) Sauter mean droplet at different rotational speeds. Reprinted with permission from Ref. [37], copyright 2013, John Wiley and Sons.

model based on the three-dimensional Maxwell distribution and We of the droplet; this led to the modified breakup model shown in Eq. (5). They then evaluated the modified breakup model using the droplet size distribution measured in the laboratory Taylor–Couette apparatus, but the end effect in the experimental apparatus led to disagreement between the experiment and simulation.

$$G(v) = G(d) = K \frac{(\varepsilon d)^{1/3}}{d} \left[\operatorname{erfc}(\Phi) + \frac{2}{\pi^{1/2}} \Phi^{1/2} \exp(-\Phi) \right]. \quad (5)$$

The droplet coalescence model was first proposed by Coulaloglou and Tavlarides [48] to describe the coalescence process between droplets in a stirred liquid. Studies have shown that whether droplets can finally coalesce into large droplets needs to satisfy two conditions: the first is whether two droplets can collide and contact, which depends on the number density of droplets; the second is the probability of coalescence under the premise of being able to collide, which is mainly influenced by the contact time, interface strength, and other factors. In the oil–water dispersion system, many droplets may collide and coalesce with each other. Therefore, the collision frequency $h(d_1, d_2)$ and the coalescence efficiency $\lambda(d_1, d_2)$ are usually used to describe and

calculate the coalescence frequency of droplet groups as shown in Eq. (6).

$$\Gamma(d_1, d_2) = h(d_1, d_2) \cdot \lambda(d_1, d_2). \quad (6)$$

Here, d_1 and d_2 are the diameters of two droplets colliding with each other. The high dispersed phase hold-up leads to a high coalescence efficiency. The coalescence efficiency at the larger droplet size is less than that at the smaller droplet size. In addition, the very high turbulent energy dissipation in the annular region leads to a generally low coalescence efficiency [40]. A device for observing the droplet coalescence and separation process under centrifugal force field was developed (Fig. 7). This process enables mixing and separation of liquid–liquid two phases. In Figs. 7(c) and 7(d), the dotted-dashed lines represent measurements in the centrifugal field and the dots with dotted lines represent measurements in the gravitational field. Sedimentation is a nonlinear process that can be attributed to a decrease in centrifugal force. Sedimentation within the centrifugal force field starts earlier and coalescence starts later compared to the gravitational field. The sedimentation and coalescence curves cross each other as the separation proceeds [50].

Studies of individual droplet behavior can reveal the droplet breakup and coalescence mechanism, but only a

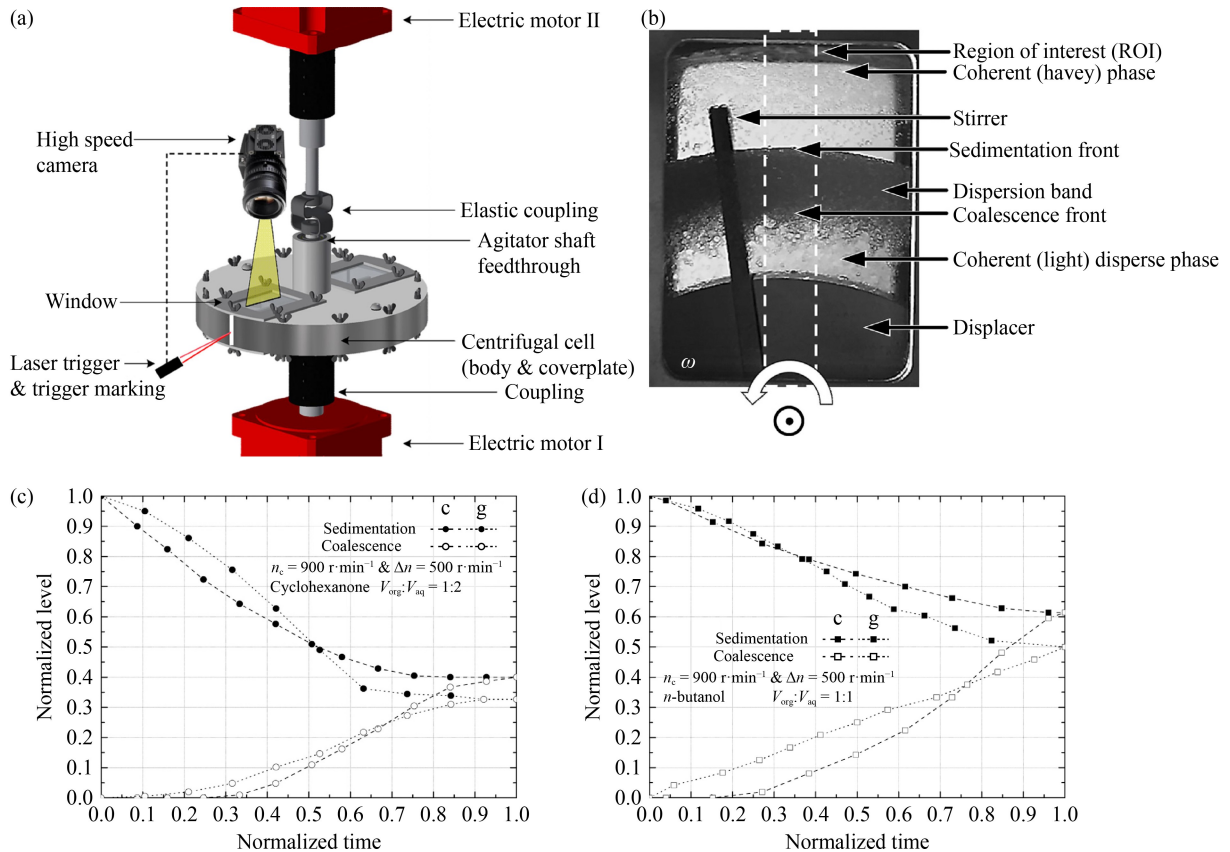


Fig. 7 (a) Experimental setup for the observation of sedimentation and coalescence; (b) photographic region for evaluation of mixing and separation process; (c) sedimentation and coalescence curve for cyclohexanone–water system ($V_{org}:V_{aq} = 1:2$); (d) sedimentation and coalescence curve for *n*-butanol–water system ($V_{org}:V_{aq} = 1:1$). Reprinted with permission from Ref. [50], copyright 2017, Elsevier.

few scholars have investigated the droplet behavior in the annular region. Rapid nuclear magnetic resonance imaging was used to investigate the effect of different surfactants on droplet deformation in the Taylor vortices. The results showed that the addition of Tween 80 increased droplet deformation in response to shear, while the addition of peptide biosurfactants reduced droplet deformation. This can be attributed to the interfacial film formed by the biosurfactant [51]. Figure 8 shows the apparatus used to observe the droplet behavior and droplet behavior in annulus. The trajectories of droplets at

different Re were traced via a high-speed camera, and the droplet trajectories were generally classified as circular, annular, or three-dimensional annular. The droplet deformations at different locations in the flow field were captured (Fig. 8(b)). The authors observed the ethanol droplet was dispersed into multiple micron-sized droplets during the sudden start-up of the device and subsequently coalesced after the flow field was stabilized. To further reveal the coalescence process within the annular gap, the droplet size variation with time was investigated using PDPA and divided into four stages according to time [52].

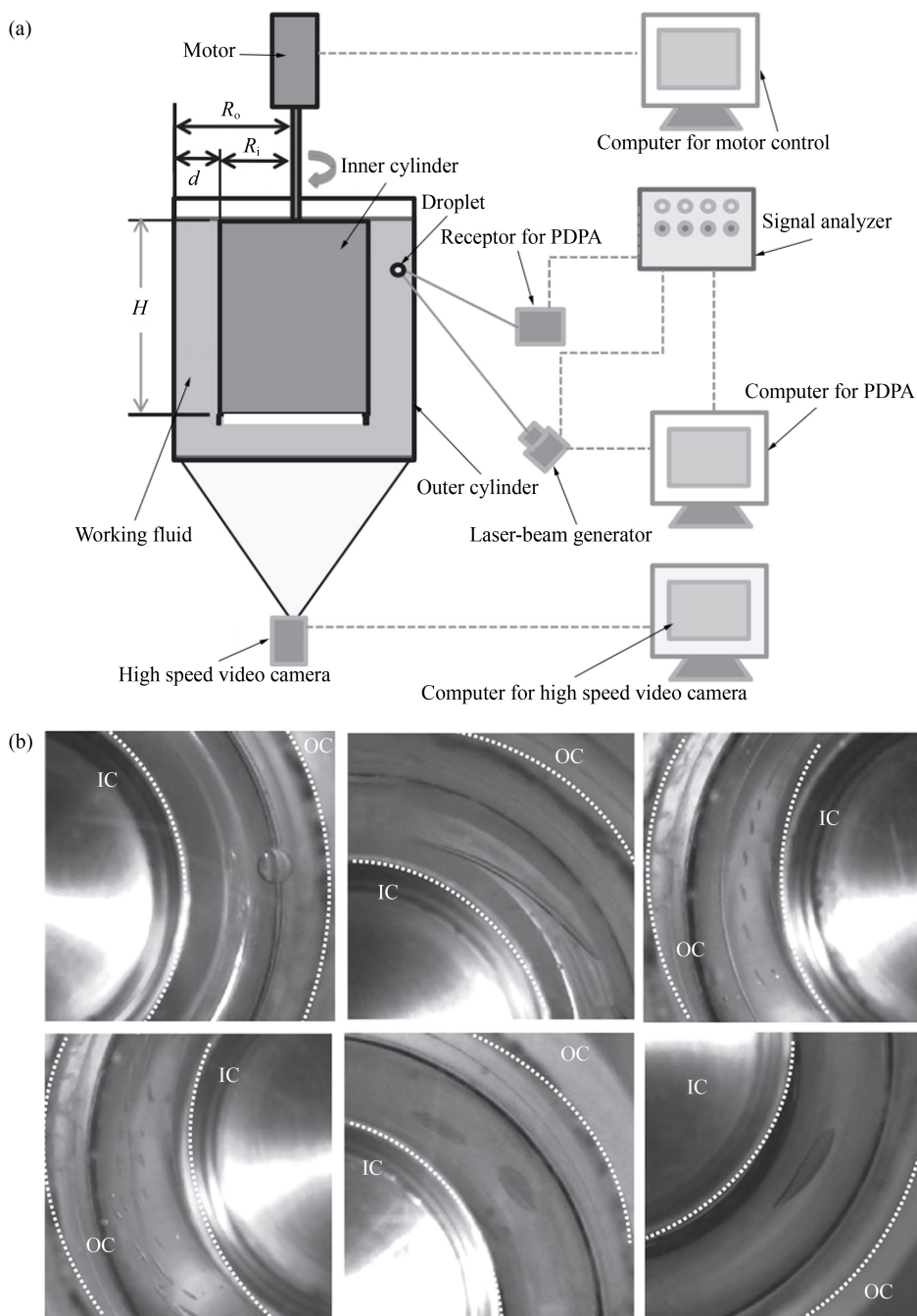


Fig. 8 (a) Experimental setup for droplet behavior studies in the annulus; (b) breakup and coalescence of the organic droplet in the annulus. Reprinted with permission from Ref. [52], copyright 2014, Elsevier.

Studies of the breakup and coalescence behavior of dispersed phase droplets using the population balance model (PBM) has also received recent attention. Wardle [53] used CFD-PBM for the first time to perform liquid–liquid mixing simulations within the mixing region of ACE. The simulation results showed that the liquid level in the case of straight vanes is twice as high as in the case of curved vanes, and the droplet size is also significantly smaller in the case of four straight vanes than in the curved vane case. A new method for multiphase flow simulation called GEneralized Multifluid Modelling Approach (GEMMA) has been used to simulate the extraction process within ACE [36]. GEMMA coupled with PBM can obtain the droplet size distribution of the organic phase, and the simulation results agree well with experimental results.

2.4 Residence time distribution

The residence time refers to the time that a liquid experiences from when it enters the system to when it leaves the system. The micromixing and macromixing of the fluid are important factors affecting the performance of the mixer. The RTD is a macroscopic representation of micromixing and is closely related to the flow pattern within the ACE. Therefore, it is of great value to study the RTD of the ACE. In practical industrial applications, dead zones, bypasses, and recirculation in ACE leads to flow patterns that deviate from the ideal flow situation, thus making the liquid residence time in ACE uneven and forming the fluid RTD.

The functions describing liquid RTD include RTD density function $E(t)$ and RTD function $F(t)$. The RTD curve reflects the overall flow pattern of the liquid phase in the ACE. The ACE can be divided into three different regions in space: the annular region where the two phases are intensively mixed, the rotating cylinder region where the two phases are settled by centrifugal separation, and the heavy phase weir and light phase weir region where the two phases are separated. The overall RTD of ACE is determined by the flow pattern in each of these regions [41]. The RTD measurement in ACE usually adopts the tracer method, and the tracer is input into a stable flow system leading to a change in the tracer content in the outflow at the outlet; this can be used to determine the residence time of the material. Generally, the $E(t)$ is obtained by the pulse method, and $F(t)$ is obtained by the step method. Compared with the step method, the pulse method uses less tracer dosage. The directly obtained $E(t)$ curve is easier to distinguish the mixing characteristics than the $F(t)$ curve [54]. The tracer should be miscible with the main fluid and have similar physical properties to the main fluid. Meanwhile, the tracer should not chemically react with the main fluid substance nor be absorbed by the container wall; it should not affect the hydrodynamic characteristics. $E(t)$ can then be calculated

via the following:

$$E(t) = \frac{C(t)}{\sum C(t)\Delta t}, \quad (7)$$

where $C(t)$ is the variation of the outlet detection tracer concentration with time. The main models to describe the degree of fluid back-mixing in ACE are the dispersion model and the tanks in series (TIS) model. The dispersion model is based on the plug flow model with the addition of axial diffusion D . The dispersion model is used to describe a non-ideal flow model with a low degree of back-mixing. The residence time in ACE can be evaluated by the dimensionless parameter Peclet number ($Pe = UL/D$) [55]. A smaller Pe is more similar to the ideal continuous stirred tank reactor. A larger Pe is more similar to the ideal plug flow reactor. The dispersion model equation is as follows:

$$E(\theta) = \frac{1}{2\sqrt{\pi\theta^3/Pe}} e^{-\frac{(1-\theta)^2}{4\theta/Pe}}, \quad (8)$$

$$\sigma_\theta^2 = \frac{2}{Pe} + \frac{8}{Pe^2}, \quad (9)$$

where σ_θ^2 is the dimensionless variance ($\sigma_\theta^2 = \frac{\sigma^2}{\tau^2}$), τ is the mean residence time, and σ^2 is the variance of RTD.

The TIS model is a flow model that uses N ideal complete mixing flow series in combination to simulate non-ideal flow. The RTD equation and variance using the TIS model are as follows [56]:

$$E(\theta) = \frac{N^N}{(N-1)!} \theta^{N-1} e^{-N\theta}, \quad (10)$$

$$\sigma_\theta^2 = \frac{1}{N}, \quad (11)$$

where θ is the ratio of time to mean residence time. The presence of severe trailing in the RTD curve indicates the presence of a dead zone in the ACE. The upper part of the rotor near the interface may be a dead zone, and hold-up in the collector may also short-circuit near the outlet, thus making most of the collector become of the dead zone. The standard TIS model does not fit well due to the trailing. A better fit can be achieved using a TIS model with a dead zone [32,41].

The factors affecting RTD in ACE include total throughput, rotational speed, flow ratio, and ACE geometry. The residence time usually decreases as the total throughput increases. Increased rotational speed leads to increased back mixing. The suction force of the rotor increases as the rotational speed increases, thus resulting in a decrease in residence time. The aspect ratio Γ has an intense influence on the flow pattern in the annular region. At very high aspect ratios, the size of the vortices is usually equal to the width of the annular gap between the cylinders. When the Γ is small (increasing the width of the

annular gap or decreasing the height of the annular gap), the end effect will change the size of the vortices and reduce the total number of vortices in the flow field. Therefore, the variation of the Γ can affect the RTD.

Figure 9 illustrates the effect of geometry on residence time in ACE. Figure 9(a) shows that the mean residence time in ACE increases as the Γ increases [57]. This result is also similar to the simulation results of the annular Taylor–Couette extractor by Vedantam et al. [58]. The addition of radial and helical baffles in the annulus can significantly reduce the degree of back mixing in ACE (Fig. 9(b)) [55,57]. The axial mixing observed at the larger baffle pitch is higher than that observed in the smaller pitch. This phenomenon can be attributed to the higher number of vortices formed in the case of a smaller baffle pitch.

3 Structural optimization of ACE

The hydrodynamic characteristics of ACE depend on such factors as the aspect ratio of the annulus, diameter of the rotor, the height of the bottom vane, two-phase flow rate, rotor speed, and diameter of the weir [59–61]. Researchers have made several improvements to the ACE structure for the process requirements in different industrial applications including modular design, magnetic drive, naturally adjustable overflow structure, self-cleaning rotor, low mixing, and reflux structure. These optimizations have improved the safety, disassembly, and reliability of the equipment during multistage operation and simplified the cleaning of solid particles in the rotor [15]. Modification of the ACE structure mainly used experimental and numerical simulations to improve the hydrodynamic behavior within the ACE to improve the extraction performance (Table 5).

3.1 Structural optimization in the mixing region

The mixing zone of the ACE includes the annular region and the mixing vane region at the bottom. Mass transfer

and hydrodynamic performance of the ACE can be improved by optimizing the mixing zone structure. The addition of the recirculation pipe on the fixed outer cylinder increases the liquid residence time in the annular region [62]. The addition of the inclined overflow pipes to the fixed outer cylinder increases the liquid flood capacity of ACE and reduces the risk of mixed liquid overflow to the light phase collector [63].

Studies on the effect of different numbers and shapes of bottom vanes on flow characteristics of ACE showed that four straight vanes had higher hold-up and liquid levels versus eight straight vanes and eight curved vanes. The mean diameter of the droplets was significantly smaller with four straight vanes than with eight curved vanes [39,64]. Therefore, the design of four straight blades has better mixing performance under low flow rate conditions. Eight straight blades or curved blades should be used to prevent liquid overflow to the light phase collector under high flow rate conditions.

The annular geometry significantly affects the flow characteristics within the ACE including shear rate, residence time, and flow pattern. Although the standard inner wall of the outer cylinder is designed with a smooth surface, improvements in the design of ribbed plates have also been investigated. The addition of horizontal radial or helical baffles in the annular region makes the RTD of ACE narrower and more similar to the ideal plug flow. Meanwhile, the ribbed design enables to stabilize the vortex and reduces axial mixing [55,57,65,66]. Thus, the ribbed design is beneficial for extraction processes requiring long residence times or low axial flow rates.

In addition, the influence of each structural parameter on the extraction efficiency is not independent but rather is the result of interaction [67]. Therefore, the correlation between each structural parameter should be considered during structural optimization of ACE.

3.2 Structural optimization in the separation region

The separation region of ACE includes the rotor, the upper weir region, and the collector. The separation during two-phase liquid can be improved by optimizing

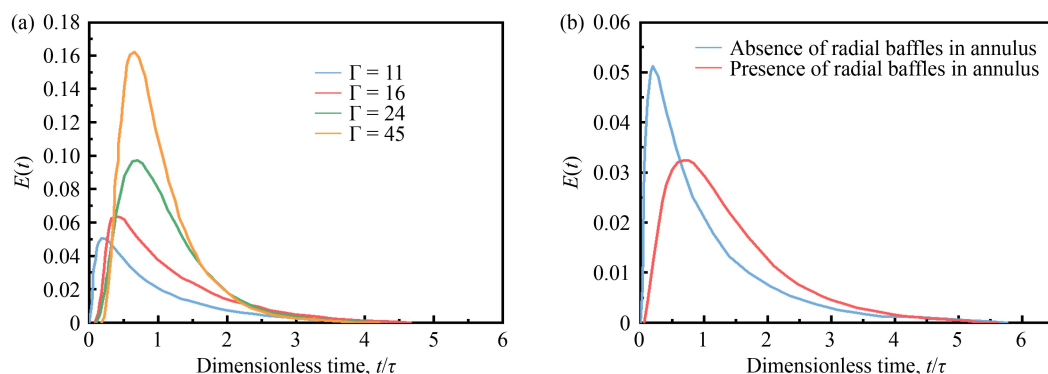
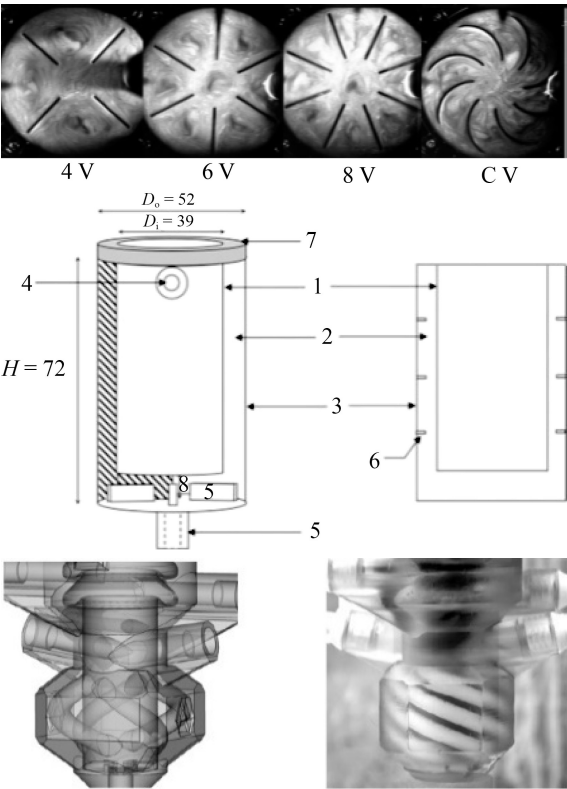
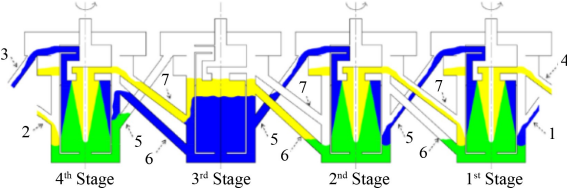
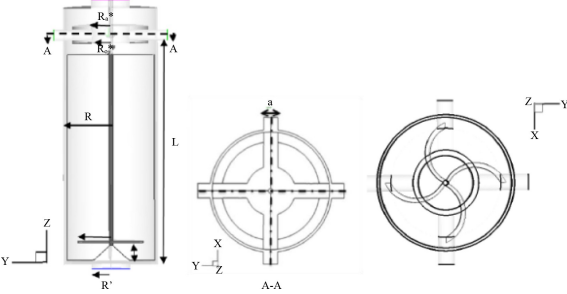
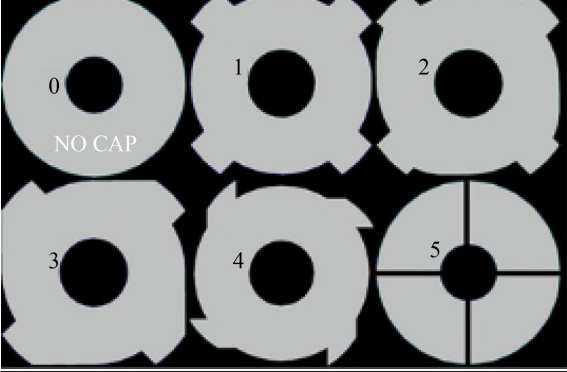


Fig. 9 (a) RTD curve under different aspect ratios; (b) effect of ribbed design on RTD. Reprinted with permission from Ref. [57], copyright 2008, American Chemical Society.

Table 5 Structure optimization of ACE in recent years

Schematic illustration	Main conclusion	Ref.
 <p>(1) Four straight vanes have a larger hold-up and higher liquid level than eight straight vanes and eight curved vanes; (2) The mean diameter for four straight vanes is significantly decreased versus eight curved vanes</p> <p>[39,64]</p> <p>(1) The ribbed design makes the RTD of the ACE narrower and more similar to an ideal plug flow; (2) The ribs stabilize the vortex and reduce axial mixing</p> <p>[55,57,66]</p> <p>The recirculation tube design increases the residence time in the mixing zone</p> <p>[62]</p>		
 <p>(1) The inclined overflow pipe structure has a higher flooding capacity compared to the horizontal overflow pipe structure; (2) The operating flux of the inclined overflow pipe design is much higher than the horizontal overflow pipe design under rotor damage conditions</p> <p>[63]</p>		
 <p>The curved blade design has a significant impact on the pressure drop, hold-up, and interface radius of the rotor; it requires less energy than straight blades</p> <p>[69]</p>		
 <p>Design 3 is more stable and less likely to form a liquid seal compared to other design</p> <p>[28,31]</p>		

the structure of the separation region. The radius of the heavy phase weir adjusting the liquid–liquid interface is the most critical parameter in the design of the centrifugal extractor. Severe phase entrainments can occur under unsuitable heavy phase weir radius conditions. The rotor inlet diameter affects the gas–liquid interface within the rotor, thus resulting in differences in separation efficiency. At the optimal rotor inlet diameter, the absolute value of the tangential velocity at each section was the highest among the tested diameter; the liquid more easily flowed towards the cylinder wall with a better separating effect. When the radial velocity relative to the rotary cylinder was positive, it was often the maximum relative velocity, thus indicating that the liquid passing the cylinder entrance can be thrown to the sidewall resulting in better separation [68].

The shape of the separating vanes in the rotor has a tremendous effect on the pressure drop, hold-up in the rotor, and the radius of the gas–liquid interface. Meanwhile, the curved vanes require less energy consumption than straight vanes [26,69]. In the heavy phase weir, the water droplets are thrown out by centrifugal force with a smaller tangential velocity than the rotor velocity. Droplets hit the upper part of the weir cover after being ejected. The droplets then gather under the weir cover and accumulate into a film on the back of the exit channel. The formation of this liquid film is generated by the improper design of the weir cover, which is a manifestation of poor liquid outflow and may eventually develop into a water seal phenomenon [28]. According to this situation, Gandhir and Wardle [31] designed different forms of the exit of the heavy phase weir and finally described a stable structure that is less likely to form a liquid seal improved design. Thus, the design modification revealing the internal flow phenomenon to discover the deficiencies of the equipment is a feasible way to optimize the equipment. The study above optimized different key components and parameters of the centrifugal extractor and is a good reference for the design of the centrifugal extractor.

4 Recent advances in the application of ACE

4.1 Hydrometallurgy

In the hydrometallurgical industry, ACE can separate target products by allowing one element with a fast mass transfer rate to be extracted while elements with a slow mass transfer rate are largely left unextracted due to the short residence time. ACE can extract heavy metals such as copper, chromium, and vanadium [8,70]. Recently, a new process was proposed for recovering light metal lithium from salt lake brines as depicted in Fig. 10. The results showed that the extraction rate of lithium under optimized conditions could reach 90.05% after five-stage ACE extraction; the lithium stripping extraction rate was close to 100% [71].

ACE offers rapid separation, good adaptability to phase ratio change, high enrichment, and low hold-up. ACE can also separate substances with significant differences in mass transfer rate but that are challenging to separate via the equilibrium extraction process. That is, ACE achieves non-equilibrium extraction separation. Therefore, ACE is particularly suitable for the extraction and separation of rare earth metals. The centrifugal extraction technique can significantly reduce the production area, working volume, number of equipment, and cost owing to lower extractant losses compared to box-type extraction equipment [72]. The concentration of rare earth can be increased from $1 \text{ g}\cdot\text{L}^{-1}$ to more than $100 \text{ g}\cdot\text{L}^{-1}$ by centrifugal extraction [73]. For non-equilibrium centrifugal extraction of rare earth concentrates from wet-process phosphoric acid, the separation factor can be increased from 0.07 to 17.6 under optimal conditions compared to equilibrium extraction [74]. A method for separating rare earth components from phosphogypsum using ACE was successfully applied in pilot plant tests and resulted in a 30%–40% reduction in manufacturing costs due to reduced solvent losses alone versus a mixer-settler [72]. Advancements in ACE manufacturing technology, remote control

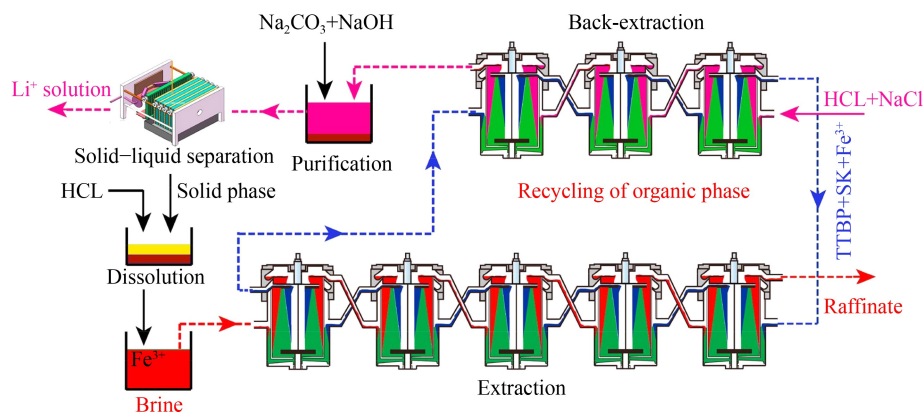


Fig. 10 Schematic diagram of lithium extraction by continuous ACE technique. Reprinted with permission from Ref. [71], copyright 2018, Elsevier.

technology, and centrifugal extraction technology in the field of rare earth separation will be further evaluated.

4.2 Reprocessing of nuclear fuel

The nuclear fuel reprocessing process generates a large amount of highly radioactive waste liquids. ACE offers a short residence time, thus facilitating nuclear criticality safety and mitigating irradiation degradation of the extractant; thus, it is widely used in the nuclear industry. ACE has been applied in various nuclear solvent extraction processes in the United States, Japan, France, and China [15]. Most applications of ACE in the nuclear industry have remained in laboratory-scale testing [9,10,75,76]. Duan et al. [77] from Tsinghua University applied an industrial-scale ACE with magnetically coupled rotors to the TPRO process and showed high mass transfer and hydrodynamic performance. Takeuchi et al. [78] from the Japan Atomic Energy Agency applied an industrial-scale ACE cascade system to uranium extraction and stripping. The results showed that the extraction stage efficiency could reach nearly 100%, and the stripping stage efficiency was 97%–98%.

These applications have achieved satisfactory results and valuable operating experiences and contribute significantly to the further development and application of ACE in the nuclear industry. However, the ACE also has a complex structure, difficult remote maintenance and replacement, and the accumulation of solid particles in the rotor—these features affect their application in industrial production. Therefore, researchers have developed ACEs with remote maintenance, remote replacement, and clean-in-place rotor designs [59,79,80]. These improved ACEs should be gradually applied to industrial-scale nuclear fuel reprocessing in the future.

4.3 Bioextraction

The process of adding a selected solvent to a mixture containing a target bioproduct and separating the desired components according to the solubility of the different components of the mixture in the solvent is called bioextraction. ACE has been widely used in the field of bioextraction because of its short residence time, which allows the target bioproduct to be extracted while other components are not extracted. A multistage model was proposed to investigate the effect of operating parameters on mass transfer efficiency for the selective extraction of epigallocatechin from tea polyphenols by applying 20 cascade ACEs [81]. The results showed that the purity and yield of epigallocatechin could reach 100% and 94% under optimal conditions, which is consistent with the results predicted by the model. In addition, centrifugal extraction techniques have been applied to recover lignin from sesame oil and to extract biophenol from extra virgin olive oil with satisfactory results [82,83]. Recently, ultrasound-assisted centrifugal extraction (UACE) tech-

nology was developed and used to extract natural products from plants [84–86]. This device (Fig. 11) includes a mixing zone and a separation zone and offers high extraction efficiency, high separation purity, and good facilitation of product processing.

4.4 Catalytic reaction

Batch production is a new technology for fine chemical manufacturing—the reactors show versatility for different processes. However, batch reactors have huge drawbacks: several batch runs must be performed for high volume production, which often leads to unstable quality and performance of the product across batches. The advantages of applying continuous ACE are multifold [87]: (1) the high mass transfer rate in the annular region is favorable for catalytic reactions; (2) the separation of the two phases is achieved in the rotor after mixing, thus eliminating the need for a subsequent liquid–liquid separation step. The main problem with applying ACE to catalytic reactions is that the short residence time leads to uncontrolled reactions that can be easily solved via ACE cascade approach.

Biodiesel can be continuously produced from sunflower oil using ACE. Here, the production rate was increased by $19 \text{ kg} \cdot \text{m}^{-3} \cdot \text{min}^{-1}$ compared to the typical batch process under optimal conditions [87,88]. For the synthesis of fatty acid ethyl esters (FAEEs) from jatropha oil by applying sodium acetate as the catalyst in a continuous ACE, batch production rates of $112 \text{ kg} \cdot \text{m}^{-3} \cdot \text{min}^{-1}$ can be reached under optimized conditions with a reproducible FAEE yield of 98 mol% [89]. Meanwhile, the synthesis and refinement of fatty acid methyl esters could be achieved using a two-stage cascade ACE [90]. A new biodiesel wet wash process was proposed based on the centrifugal extraction technique, and 17 kJ equipment

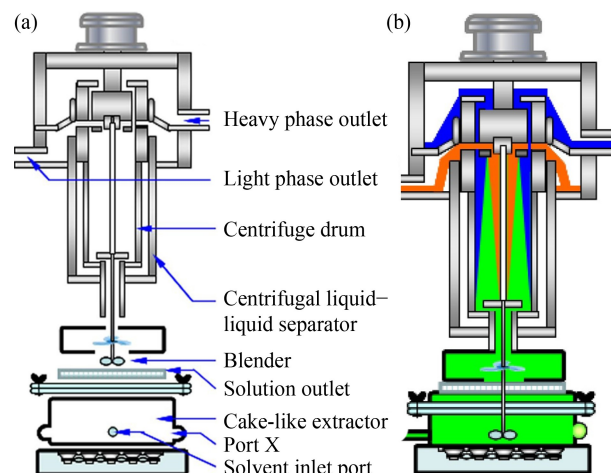


Fig. 11 (a) Schematic diagram of the UACE structure. Reprinted with permission from Ref. [84], copyright 2021, Elsevier. (b) Status of operating of UACE. Reprinted with permission from Ref. [86], copyright 2021, Elsevier.

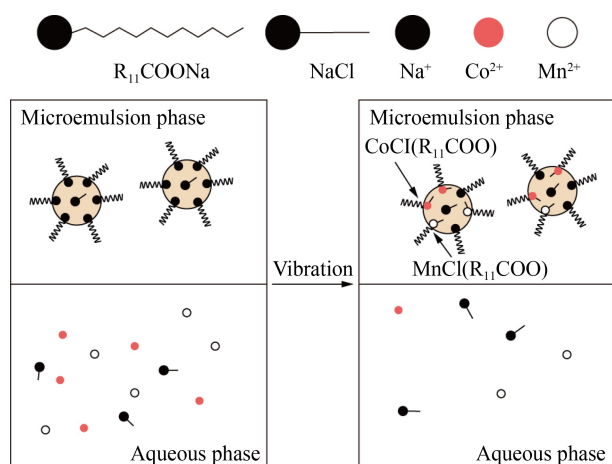


Fig. 13 Schematic diagram of microemulsion extraction mechanism. Reprinted with permission from Ref. [100], copyright 2018, Elsevier.

pollutant components such as suspended particles, oil, organic pollutants, and heavy metals. It is challenging to meet the standards of water quality regulations using only a single treatment technology. Therefore, hybrid processes combining ACE technology with other wastewater treatment technologies should be considered in the future.

5 Conclusions and future prospects

Relative to extraction columns and mixer-settlers, ACE has the advantages of compact structure, short residence time, high mass transfer rate, and high separation efficiency. Researchers have extensively studied hydrodynamic behavior to solve the many problems of ACE in industrial applications and promote the development of centrifugal extraction technology. Meanwhile, some structure modification of the ACE was performed to improve the mixing and separation performance in specific industrial applications. Recently, ACE has been applied in various fields with satisfactory results, and its application has been broadened to some new fields. The following issues need to be considered in the future to drive the further development of ACE technology.

The liquid–liquid two-phase flow inside the annulus has been relatively well understood, but studies of the multiphase flow field inside the rotor is still mainly adopted by numerical simulations due to the difficulties in making direct observations. Only Eggert et al. [101] used computed tomography technology to measure the liquid–liquid two-phase flow field inside the rotor. Thus, the multiphase flow field inside the rotor should be further investigated in the future by using advanced measurement methods.

The droplet breakup mechanism in the annular region and the coalescence mechanism inside the rotor is still not deep enough to explain phenomena such as droplet

breakup during sudden equipment start-up. Future work should consider a combination of experimental and numerical simulations to study the breakup and coalescence behavior of one droplet in ACE. Uncovering of the breakup and coalescence mechanisms can provide theoretical guidance for predicting the mass transfer and separation performance of ACE.

The structure of the ACE has been optimized using numerical simulations and hydrodynamic tests to improve the hydrodynamic characteristics. Further structural modification should be carried out for the specific processes in the future. In addition, most ACEs are currently manufactured using stainless steel that is susceptible to corrosion even in extreme conditions. Therefore, functional materials suitable for extreme conditions should be considered for the processing and manufacturing of ACE.

ACE has been widely used in hydrometallurgy, nuclear fuel reprocessing, bioextraction, catalytic reaction, and wastewater treatment due to its excellent hydrodynamic and mass transfer performance. However, most of these applications remain in the laboratory scale stage, and the search for reasonable scaling methods and studies of stability and reliability after scaling-up is the focus of future research in this field. The application of ACE should be further promoted in new fields.

Enhancement of mass transfer performance by employing external fields such as magnetic fields and ultrasonic waves has also been demonstrated in extraction columns. However, magnetic field-assisted ACE technology and ultrasonic-coupled ACE technology have not yet received sufficient attention. Therefore, future work should also investigate the effect of magnetic field or ultrasound on the mass transfer rate and separation efficiency of ACE by adding magnetic nanoparticles or using an ultrasonic generation device.

Acknowledgments We gratefully acknowledge the financial support from the National Natural Science Foundation of China (Grant No. 22078102) and the Shanghai Sailing Program, China (Grant No. 21YF1409500).

References

1. Heredia V, Pruvost J, Gonçalves O, Drouin D, Marchal L. Lipid recovery from *nannochloropsis gaditana* using the wet pathway: investigation of the operating parameters of bead milling and centrifugal extraction. *Algal Research*, 2021, 56: 102318
2. Deshpande J B, Navale G R, Dhame M S, Kulkarni A A. Continuous interfacial centrifugal separation and recovery of silver nanoparticles. *Chemical Engineering & Technology*, 2020, 43(3): 582–592
3. Zhang P L, Wang S C, Tang K W, Xu W F, Qiu Y R, Xiong B Q, Liu Y. Multistage enantioselective reactive extraction of terbutaline enantiomers by hydrophobic phase transfer: experiment and modeling. *Separation and Purification Technology*, 2018, 191: 208–215

4. Zhang P L, Wang S C, Tang K W, Xu W F, He F, Qiu Y R. Modeling multiple chemical equilibrium in chiral extraction of metoprolol enantiomers from single-stage extraction to fractional extraction. *Chemical Engineering Science*, 2018, 177: 74–88
5. Zhang P L, Feng X F, Tang K W, Xu W F. Study on enantioseparation of α -cyclopentyl-mandelic acid enantiomers using continuous liquid–liquid extraction in centrifugal contactor separators: experiments and modeling. *Chemical Engineering and Processing*, 2016, 107: 168–176
6. Tang K W, Wang Y Q, Zhang P L, Huang Y, Hua J. Optimization study on continuous separation of equal enantiomers using enantioselective liquid–liquid extraction in centrifugal contactor separators. *Process Biochemistry*, 2016, 51(1): 113–123
7. Jing X H, Ning P G, Cao H B, Sun Z, Wang J Y. Separation of V(V) and Cr(VI) in leaching solution using annular centrifugal contactors. *Chemical Engineering Journal*, 2017, 315: 373–381
8. Jing X H, Wang J Y, Cao H B, Ning P G, Sun Z. Rapid selective extraction of V(V) from leaching solution using annular centrifugal contactors and stripping for NH_4VO_3 . *Separation and Purification Technology*, 2017, 187: 407–414
9. Miao Q D, Sun T X, Chen H L, Zheng Q, Duan W H. Comparison of the hydraulic characteristics of the 30% TRPO/kerosene- HNO_3 and iPr-C[4]C-6/*n*-octanol- HNO_3 systems in an annular centrifugal extractor. *Progress in Nuclear Energy*, 2021, 136: 103734
10. Mohapatra P K, Verma P K, Prabhu D R, Raut D R. Extraction of ^{137}Cs from acidic feed by centrifugal contactors using a solution of calix[4]arene-bis-1,2-benzo-crown-6 in phenyltrifluoromethyl sulphone. *Nuclear Technology*, 2019, 205(8): 1119–1125
11. Schuur B, Winkelmann J G M, de Vries J G, Heeres H J. Experimental and modeling studies on the enantio-separation of 3,5-dinitrobenzoyl-(R),(S)-leucine by continuous liquid–liquid extraction in a cascade of centrifugal contactor separators. *Chemical Engineering Science*, 2010, 65(16): 4682–4690
12. Bernstein G, Grosvenor D, Lenc J, Levitz N. A high-capacity annular centrifugal contactor. *Nuclear Technology*, 1973, 20(3): 200–202
13. Vedantam S, Joshi J B. Annular centrifugal contactors—a review. *Chemical Engineering Research & Design*, 2006, 84(7): 522–542
14. Vedantam S, Wardle K E, Tamhane T V, Ranade V V, Joshi J B. CFD simulation of annular centrifugal extractors. *International Journal of Chemical Engineering*, 2012, 2012: 759397
15. Duan W H, Zhao M M, Wang C Q, Cao S. Recent advances in the development and application of annular centrifugal contactors in the nuclear industry. *Solvent Extraction and Ion Exchange*, 2014, 32(1): 1–26
16. Jing X H, Ning P G, Cao H B, Wang J Y, Sun Z. A review of application of annular centrifugal contactors in aspects of mass transfer and operational security. *Hydrometallurgy*, 2018, 177: 41–48
17. Joseph D D, Nguyen K, Beavers G S. Non-uniqueness and stability of the configuration of flow of immiscible fluids with different viscosities. *Journal of Fluid Mechanics*, 1984, 141: 319–345
18. Campero R J, Vigil R D. Spatiotemporal patterns in liquid–liquid Taylor–Couette–Poiseuille flow. *Physical Review Letters*, 1997, 79(20): 3897–3900
19. Zhu X, Vigil R D. Banded liquid–liquid Taylor–Couette–Poiseuille flow. *AIChE Journal*. American Institute of Chemical Engineers, 2001, 47(9): 1932–1940
20. Sathe M J, Deshmukh S S, Joshi J B, Koganti S B. Computational fluid dynamics simulation and experimental investigation: study of two-phase liquid–liquid flow in a vertical Taylor–Couette contactor. *Industrial & Engineering Chemistry Research*, 2010, 49(1): 14–28
21. Campbell C, Olsen M G, Dennis Vigil R. Flow regimes in two-phase hexane/water semibatch vertical Taylor vortex flow. *Journal of Fluids Engineering*, 2019, 141(11): 111203
22. Campbell C, Olsen M G, Vigil R D. Jet breakup regimes in liquid–liquid Taylor vortex flow. *International Journal of Multiphase Flow*, 2020, 131: 103401
23. Baier G, Graham M D. Two-fluid Taylor–Couette flow: experiments and linear theory for immiscible liquids between corotating cylinders. *Physics of Fluids*, 1998, 10(12): 294–303
24. Nakase M, Makabe R, Takeshita K. Relation between oil–water flow and extraction performance in liquid–liquid countercurrent centrifugal extractors with Taylor vortices. *Journal of Nuclear Science and Technology*, 2013, 50(3): 287–295
25. Chen M X, Xie T L, Xu C. Continuous counter-current centrifugal extraction column with high throughput using a spiral inner cylinder. *Chemical Engineering and Processing*, 2018, 125: 1–7
26. Xu Y, Wang J G, Zhao S L, Bai Z S. PIV experimental study on the flow field in the rotor zone of an annular centrifugal contactor. *Chemical Engineering Research & Design*, 2015, 94: 691–701
27. Patra J, Pandey N K, Muduli U K, Natarajan R, Joshi J B. Hydrodynamic study of flow in the rotor region of annular centrifugal contactors using CFD simulation. *Chemical Engineering Communications*, 2013, 200(4): 471–493
28. Wardle K E, Allen T R, Swaney R. CFD simulation of the separation zone of an annular centrifugal contactor. *Separation Science and Technology*, 2009, 44(3): 517–542
29. Yang X Y. Study on synergetic treatment of sodium sulfate wastewater from coal tar processing by ternary solvent and centrifugal extraction. Dissertation for the Doctoral Degree. Shanghai: East China University of Science and Technology, 2019, 97–106 (in Chinese)
30. Li S W, Duan W H, Chen J, Wang J C. CFD simulation of gas–liquid–liquid three-phase flow in an annular centrifugal contactor. *Industrial & Engineering Chemistry Research*, 2012, 51(34): 11245–11253
31. Gandhir A, Wardle K E. CFD analysis of fluid flow above the upper weir of an annular centrifugal contactor. *Separation Science and Technology*, 2012, 47(1): 1–10
32. Ayyappa S V N, Balamurugan M, Kumar S, Kamachi Mudali U. Mass transfer and hydrodynamic studies in a 50 mm diameter centrifugal extractor. *Chemical Engineering and Processing*,

- 2016, 105: 30–37
33. Kadam B D, Joshi J B, Koganti S B, Patil R N. Dispersed phase hold-up, effective interfacial area and Sauter mean drop diameter in annular centrifugal extractors. *Chemical Engineering Research & Design*, 2009, 87(10): 1379–1389
34. Davis M W, Weber E J. Liquid–liquid extraction between rotating concentric cylinders. *Industrial & Engineering Chemistry*, 1960, 52(11): 929–934
35. Grafschaffter A, Siebenhofer M. Design rules for the Taylor–Couette disc contactor. *Chemie Ingenieur Technik (Weinheim)*, 2017, 89(4): 409–415
36. De Santis A, Hanson B C, Fairweather M. Hydrodynamics of annular centrifugal contactors: a CFD analysis using a novel multiphase flow modelling approach. *Chemical Engineering Science*, 2021, 242: 116729
37. Wyatt N B, O’Hern T J, Shelden B. Drop-size distributions and spatial distributions in an annular centrifugal contactor. *AIChE Journal*. American Institute of Chemical Engineers, 2013, 59(6): 2219–2226
38. Campbell C, Olsen M, Vigil R. Droplet size distributions in liquid–liquid semi-batch Taylor vortex flow. *AIP Advances*, 2020, 10(8): 085316
39. Wardle K E. Liquid–liquid mixing studies in annular centrifugal contactors comparing stationary mixing vane options. *Solvent Extraction and Ion Exchange*, 2015, 33(7): 671–690
40. Tamhane T V, Joshi J B, Mudali K, Natarajan R, Patil R N. Measurement of drop size characteristics in annular centrifugal extractors using phase doppler particle analyzer (PDPA). *Chemical Engineering Research & Design*, 2012, 90(8): 985–997
41. Schuur B, Kraai G N, Winkelman J G M, Heeres H J. Hydrodynamic features of centrifugal contactor separators: experimental studies on liquid hold-up, residence time distribution, phase behavior and drop size distributions. *Chemical Engineering and Processing*, 2012, 55: 8–19
42. Kumar S, Mudali K. Experimental measurements of drop size distributions in 30 mm diameter annular centrifugal contactor with 30% TBP–nitric acid biphasic system. *International Journal of Nuclear Energy*, 2013, 2013: 402505
43. Drewery S, Heeres E, Percival S, Rhodes C, George M S, Wilbers E, Woodhead D A. Experimental and modelling studies of mass transfer in centrifugal contactors. *Procedia Chemistry*, 2012, 7: 341–348
44. Nakase M, Kinuhata H, Takeshita K. Multi-staging for extraction of cesium from nitric acid by a single liquid–liquid countercurrent centrifugal extractor with Taylor vortices. *Journal of Nuclear Science and Technology*, 2013, 50(11): 1089–1098
45. Nakase M, Takeshita K. Numerical and experimental study on oil–water dispersion in new countercurrent centrifugal extractor. *Procedia Chemistry*, 2012, 7: 288–294
46. Haas P A. Turbulent dispersion of aqueous drops in organic liquids. *AIChE Journal*. American Institute of Chemical Engineers, 1987, 33(6): 987–995
47. Farzad R, Puttinger S, Pirker S, Schneiderbauer S. Investigation of droplet size distribution for liquid–liquid emulsions in Taylor–Couette flows. *Journal of Dispersion Science and Technology*, 2017, 39(2): 250–258
48. Coulaloglou C A, Tavlarides L L. Description of interaction processes in agitated liquid–liquid dispersions. *Chemical Engineering Science*, 1977, 32(11): 1289–1297
49. Eskin D, Taylor S D, Yang D. Modeling of droplet dispersion in a turbulent Taylor–Couette flow. *Chemical Engineering Science*, 2017, 161: 36–47
50. Eggert A, Sibirtsev S, Menne D, Jupke A. Liquid–liquid centrifugal separation—new equipment for optical (photographic) evaluation at laboratory scale. *Chemical Engineering Research & Design*, 2017, 127: 170–179
51. Fridjonsson E, Chandrasekera T, Sederman A J, Johns M, Zhao C, Middelberg A. Imaging the effects of peptide bio-surfactants on droplet deformation in a Taylor–Couette shear cell. *Soft Matter*, 2011, 7(6): 2961–2967
52. Qiao J, Deng R S, Wang C H. Droplet behavior in a Taylor vortex. *International Journal of Multiphase Flow*, 2014, 67: 132–139
53. Wardle K. Hybrid multiphase CFD simulation for liquid–liquid interfacial area prediction in annular centrifugal contactors. In: *Proceedings of International Nuclear Fuel Cycle Conference, GLOBAL 2013: Nuclear Energy at a Crossroads*. La Grange Park, IL: American Nuclear Society, 2013
54. Martin A D. Interpretation of residence time distribution data. *Chemical Engineering Science*, 2000, 55(23): 5907–5917
55. Tamhane T V, Joshi J B, Kamachi Mudali U, Natarajan R, Patil R N. Axial mixing in annular centrifugal extractors. *Chemical Engineering Journal*, 2012, 207–208: 462–472
56. Levenspiel O. *Chemical Reaction Engineering*. New York: John Wiley & Sons, 1999: 321–324
57. Deshmukh S S, Sathe M J, Joshi J B, Koganti S B. Residence time distribution and flow patterns in the single-phase annular region of annular centrifugal extractor. *Industrial & Engineering Chemistry Research*, 2009, 48(1): 37–46
58. Vedantam S, Joshi J B, Koganti S B. CFD Simulation of RTD and mixing in the annular region of a Taylor–Couette contactor. *Industrial & Engineering Chemistry Research*, 2006, 45(18): 6360–6367
59. Duan W H, Sun T X, Wang J H. Separation of Nd^{3+} and Fe^{3+} by non-equilibrium solvent extraction using an annular centrifugal contactor. *Separation and Purification Technology*, 2015, 146: 108–113
60. Zhao M M, Cao S, Duan W H. Effects of some parameters on mass-transfer efficiency of a $\phi 20$ mm annular centrifugal contactor for nuclear solvent extraction processes. *Progress in Nuclear Energy*, 2014, 74: 154–159
61. Bai Z S, Zhang J, Gan R W, Xu Y, Liu W J. Effect of cylinder rotation on flow characteristics of the annular region in annular centrifugal extractor. *Separation Science and Technology*, 2015, 50(6): 813–819
62. Brown M A, Wardle K E, Lumetta G, Gelis A V. Accomplishing equilibrium in ALSEP: demonstrations of modified process chemistry on 3D printed enhanced annular centrifugal contactors. *Procedia Chemistry*, 2016, 21: 167–173
63. Manavalan B, Joshi J B, Pandey N K. Design modification in the stationary bowl of annular centrifugal extractors to handle

- adverse conditions. *Industrial & Engineering Chemistry Research*, 2020, 59(25): 11757–11766
64. Wardle K E, Allen T R, Anderson M H, Swaney R E. Analysis of the effect of mixing vane geometry on the flow in an annular centrifugal contactor. *AIChE Journal*. American Institute of Chemical Engineers, 2009, 55(9): 2244–2259
 65. Deng R, Yohanes Arifin D, Ye Chyn M, Wang C H. Taylor vortex flow in presence of internal baffles. *Chemical Engineering Science*, 2010, 65(16): 4598–4605
 66. Deshmukh S S, Joshi J B, Koganti S B. Flow visualization and three-dimensional CFD simulation of the annular region of an annular centrifugal extractor. *Industrial & Engineering Chemistry Research*, 2008, 47(10): 3677–3686
 67. Su Y G, Tang J X, Yang X X, Wang R J. Effect of geometrical parameters on extraction efficiency of the annular centrifugal contactor. *Separations*, 2021, 8(102): 1–11
 68. Fan Z, Bai Z S, Xu Y, Yang X Y. Effects of centrifugal extractor cylinder inlet radius on the cylinder flow field. *Chemical Industry and Engineering Progress*, 2015, 34(5): 1232–1235 (in Chinese)
 69. Ghaya H, Guizani R, Mhiri H, Bournot P. CFD study of the effect of geometrical shape of separation blades on the rotor performance of an annular centrifugal extractor (ACE). *Journal of Applied Fluid Mechanics*, 2019, 12(4): 1189–1202
 70. Fan X B, Yu X P, Guo Y F, Deng T L. Recovery of boron from underground brine by continuous centrifugal extraction with 2-ethyl-1,3-hexanediol (EHD) and its mechanism. *Journal of Chemistry*, 2018, 2018: 7530837
 71. Yu X P, Fan X B, Guo Y F, Deng T L. Recovery of lithium from underground brine by multistage centrifugal extraction using *tri*-isobutyl phosphate. *Separation and Purification Technology*, 2019, 211: 790–798
 72. Abramov A M, Volobuev O I, Galieva Z N, Sobol' Y B, Solodovnikov A V, Yachmenov A A, Kuznetsov G I, Kosogorov A V, Trusilov N N. Separating rare-earth elements on centrifugal extractors: developing technology, designing equipment, and engineering production. *Theoretical Foundations of Chemical Engineering*, 2020, 54(4): 762–768
 73. He Q, Qiu J, Chen J F, Zan M M, Xiao Y F. Progress in green and efficient enrichment of rare earth from the leaching liquor of ion adsorption type rare earth ores. *Journal of Rare Earths*, 2021, (in press)
 74. Wang L S, Yu Y, Liu Y, Long Z Q. Centrifugal extraction of rare earths from wet-process phosphoric acid. *Rare Metals*, 2011, 30(3): 211–215
 75. Chen H L, Zheng Q, Duan W H. Hydraulic characteristics of *n*-octanol/aqueous solution systems in a 25-mm annular centrifugal extractor. *Separation Science and Technology*, 2020, 55(8): 1515–1523
 76. Chen H L, Wang J C, Duan W H, Chen J. Hydrodynamic characteristics of 30% TBP/kerosene-HNO₃ solution system in an annular centrifugal contactor. *Nuclear Science and Techniques*, 2019, 30(89): 1–12
 77. Duan W H, Sun T X, Wang J C. An industrial-scale annular centrifugal extractor for the TRPO process. *Nuclear Science and Techniques*, 2018, 29(46): 1–9
 78. Takeuchi M, Ogino H, Nakabayashi H, Arai Y, Washiya T, Kase T, Nakajima Y. Extraction and stripping tests of engineering-scale centrifugal contactor cascade system for spent nuclear fuel reprocessing. *Journal of Nuclear Science and Technology*, 2009, 46(3): 217–225
 79. Meikrantz D H, Garn T G, Law J D, Macaluso L L. A centrifugal contactor design to facilitate remote replacement. *Nuclear Technology*, 2011, 173(3): 289–299
 80. Law J D, Meikrantz D H, Garn T G, Macaluso L L. Advanced remote maintenance design for pilot-scale centrifugal contactors. *Nuclear Technology*, 2011, 173(2): 191–199
 81. Wang W R, Zhang P L, Ou J, Liu F S, Tang K W, Xu W F. Selective extraction of ECG from tea polyphenols by one step in centrifugal contactor separators: modeling and application. *Industrial & Engineering Chemistry Research*, 2019, 58(5): 2027–2035
 82. Michailidis D, Angelis A, Aligiannis N, Mitakou S, Skaltsounis L. Recovery of sesamin, sesamolin, and minor lignans from sesame oil using solid support-free liquid–liquid extraction and chromatography techniques and evaluation of their enzymatic inhibition properties. *Frontiers in Pharmacology*, 2019, 10: 1–13
 83. Angelis A, Michailidis D, Antoniadis L, Stathopoulos P, Tsantila V, Nuzillard J M, Renault J H, Skaltsounis L A. Pilot continuous centrifugal liquid–liquid extraction of extra virgin olive oil biophenols and gram-scale recovery of pure oleocanthal, oleacein, MFOA, MFLA and hydroxytyrosol. *Separation and Purification Technology*, 2021, 255: 117692
 84. Zhang Y C, Liu R Y, Liu C M, Li S N, Tsao R. Development of ultrasound-assisted mixture extraction and online extraction solution concentration coupled with countercurrent chromatography for the preparation of pure phytochemicals from *Phellinus vaninii*. *Journal of Chromatography. B, Analytical Technologies in the Biomedical and Life Sciences*, 2021, 1171: 122619
 85. Zhang Y C, Liu R Y, Liu C M, Li S N, Hou W C. Development of ultrasound-assisted centrifugal extraction combined with two countercurrent chromatography systems for the simultaneous extraction and isolation of phytochemicals. *Journal of Separation Science*, 2021, 44(11): 2279–2289
 86. Zhang Y C, Liu C M, Li S N, Hou W C, Tsao R. Development of ultrasound-assisted centrifugal extraction and online solvent concentration coupled with parallel countercurrent chromatography for the preparation of purified phytochemicals: application to *Lycium ruthenicum*. *Industrial Crops and Products*, 2021, 162: 113266
 87. Kraai G N, van Zwol F, Schuur B, Heeres H J, de Vries J G. Two-phase (bio)catalytic reactions in a table-top centrifugal contact separator. *Angewandte Chemie*, 2007, 120(21): 3969–3972
 88. Kraai G N, Schuur B, van Zwol F, van de Bovenkamp H H, Heeres H J. Novel highly integrated biodiesel production technology in a centrifugal contactor separator device. *Chemical Engineering Journal*, 2009, 154(1): 384–389
 89. Abduh M Y, van Ulden W, Kalpoe V, van de Bovenkamp H H, Manurung R, Heeres H J. Biodiesel synthesis from *Jatropha curcas* L. oil and ethanol in a continuous centrifugal contactor

- separator. *European Journal of Lipid Science and Technology*, 2013, 115(1): 123–131
90. Abduh M Y, van Ulden W, van de Bovenkamp H H, Buntara T, Picchioni F, Manurung R, Heeres H J. Synthesis and refining of sunflower biodiesel in a cascade of continuous centrifugal contactor separators. *European Journal of Lipid Science and Technology*, 2015, 117(2): 242–254
91. Fayyazi E, Ghobadian B, Safieddin Ardebili S M, Najafi G, Mousavi S M, Hosseinzadeh Samani B, Yue J. Biodiesel fuel purification in a continuous centrifugal contactor separator: an environmental-friendly approach. *Sustainable Energy Technologies and Assessments*, 2021, 47: 101511
92. Ilmi M, Klokhorst A, Winkelman J G M, Euverink G J W, Hidayat C, Heeres H J. Process intensification of catalytic liquid–liquid solid processes: continuous biodiesel production using an immobilized lipase in a centrifugal contactor separator. *Chemical Engineering Journal*, 2017, 321: 76–85
93. Fayyazi E, Ghobadian B, van de Bovenkamp H H, Najafi G, Hosseinzadehsamani B, Heeres H J, Yue J. Optimization of biodiesel production over chicken eggshell-derived CaO catalyst in a continuous centrifugal contactor separator. *Industrial & Engineering Chemistry Research*, 2018, 57(38): 12742–12755
94. Xu Y, Tang K, Bai Z S, Wang H L. Hydrodynamic and mass-transfer characteristics of annular centrifugal contactors on the caprolactam recovery from waste liquor. *Applied Mechanics and Materials*, 2013, 330: 792–798
95. Hao M M, Bai Z S, Wang H L, Liu W J. Removal of oil from electric desalting wastewater using centrifugal contactors. *Journal of Petroleum Science Engineering*, 2013, 111: 37–41
96. Yang X Y, Wang B J, Luo H Q, Yan S L, Dai J, Bai Z S. Efficient recovery of phenol from coal tar processing wastewater with tributylphosphane/diethyl carbonate/cyclohexane: extraction cycle and mechanism study. *Chemical Engineering Research & Design*, 2020, 157: 104–113
97. Yang X Y, Bai Z S, Wang B J, Jie F P. Optimal ternary extractant for phenol removal from wastewater: modeling and application. *Separation Science and Technology*, 2019, 54(1): 69–78
98. Jie F P, Bai Z S, Yang X Y. Study on extraction of cobalt(II) by sodium laurate/pentan-1-ol/heptane/NaCl microemulsion system. *Journal of Radioanalytical and Nuclear Chemistry*, 2018, 315(3): 581–593
99. Jie F P, Bai Z S, Yang X Y. Extraction of Mn(II) from NaCl solution by NaCl/sodium oleate/*n*-pentanol/*n*-heptane microemulsion system. *Separation Science and Technology*, 2018, 53(9): 1351–1360
100. Yang X Y, Jie F P, Wang B J, Bai Z S. High-efficient synergistic extraction of Co(II) and Mn(II) from wastewater via novel microemulsion and annular centrifugal extractor. *Separation and Purification Technology*, 2019, 209: 997–1006
101. Eggert A, Kogl T, Arlt W, Jupke A. Computer tomographic detection of the liquid–liquid mixing and separation within the annular centrifugal contactor/extractor. *Chemical Engineering Research & Design*, 2019, 142: 143–153